



HAL
open science

Toward improved sea ice freeboard observation with SAR altimetry using the physical retracker SAMOSA+
Antoine Laforge, Sara Fleury, Salvatore Dinardo, Florent Garnier, Frédérique Remy, Jérôme Benveniste, Jérôme Bouffard, Jonas Verley

► **To cite this version:**

Antoine Laforge, Sara Fleury, Salvatore Dinardo, Florent Garnier, Frédérique Remy, et al.. Toward improved sea ice freeboard observation with SAR altimetry using the physical retracker SAMOSA+. *Advances in Space Research*, 2021, 68, pp.732-745. 10.1016/j.asr.2020.02.001 . insu-03671336

HAL Id: insu-03671336

<https://insu.hal.science/insu-03671336>

Submitted on 18 May 2022

HAL is a multi-disciplinary open access archive for the deposit and dissemination of scientific research documents, whether they are published or not. The documents may come from teaching and research institutions in France or abroad, or from public or private research centers.

L'archive ouverte pluridisciplinaire **HAL**, est destinée au dépôt et à la diffusion de documents scientifiques de niveau recherche, publiés ou non, émanant des établissements d'enseignement et de recherche français ou étrangers, des laboratoires publics ou privés.



Distributed under a Creative Commons Attribution - NonCommercial - NoDerivatives 4.0 International License



Toward improved sea ice freeboard observation with SAR altimetry using the physical retracker SAMOSA+

Antoine Laforge^{a,*}, Sara Fleury^a, Salvatore Dinardo^b, Florent Garnier^a,
Frédérique Remy^a, Jérôme Benveniste^c, Jérôme Bouffard^c, Jonas Verley^{a,1}

^a *Laboratoire d'Etude en Géophysique et Océanographie Spatiales, Centre National de la Recherche Scientifique (LEGOS, CNRS, UMR5566), Université de Toulouse, 31400, France*

^b *HeSpace, Robert Bosch Strasse 7, 64293 Darmstadt, Germany*

^c *European Space Agency (ESA/ESRIN), 00044 Frascati, Italy*

Received 28 May 2019; received in revised form 25 January 2020; accepted 4 February 2020

Available online 19 February 2020

Abstract

Since 2010, the CryoSat-2 satellite mission has enabled to largely improve sea ice freeboard estimations. But due to the complexity of radar echoes over sea ice, freeboard retrieval from altimetry still presents some errors and biases that further limit the potential of these observations for climate studies or for assimilation into models. Various methods have been explored, producing a large range of freeboard estimations. In this study, we analyze the main steps of the radar freeboard computation developed as part of the Cryo-SeaNice Project. The objective is to quantify the impacts of each processing method and to identify optimal strategies to improve freeboard estimations from SAR altimetry measurements. We consider two SAR processing options: the Hamming Window (HW) and with the Zero-Padding (ZP), and 2 retracker: the Threshold First Maximum Retracker Algorithm (TFMRA) based on heuristic measurements and SAMOSA+ a retracker declined from model based analysis of the surface back-scatter. Four freeboard solutions are generated from combinations of the 2 processing options (HW and ZP or ZP only) and the 2 types of retracker. In addition, an alternative to the Hamming Window method to filter out side-lobes errors is presented. The impacts of the different approaches to estimate freeboard are quantified from comparisons with Operation Ice Bridge (OIB) and the Beaufort Gyre Exploration project (BGEP) *in situ* data. Our results show that SAMOSA+ provides more precise freeboard estimations. This new time-series is available on CTOH website. We also identified some impacts of the Hamming Window for both retracker. Finally, we present the potential of using the simpler threshold retracker but with a correction to account for the surface roughness that is calibrated against SAMOSA+.

© 2020 COSPAR. Published by Elsevier Ltd. This is an open access article under the CC BY-NC-ND license (<http://creativecommons.org/licenses/by-nc-nd/4.0/>).

Keywords: Sea ice freeboard; Remote sensing; Arctic; Delay-Doppler Altimetry; SAMOSA+; TFMRA; Hamming; Zero-padding

1. Introduction

For the last 25 years satellite altimetry has significantly improved our ability to observe, monitor and comprehend

physical processes of the earth system. In the cryosphere, the CryoSat-2 satellite mission (2010-), equipped with the Ku band SIRAL (SAR/Interferometric Radar Altimeter) instrument (Wingham et al., 2006; Parrinello et al., 2018), has enabled to observe sea ice thickness from space. This measurement is crucial to forecast sea ice evolutions due to climate change. For instance, the assimilation of sea ice thickness data into the MetOffice model has allowed to perform sea ice extent seasonal forecasts (Blockley and Peterson, 2018).

* Corresponding author.

E-mail addresses: antoine.laforge@legos.obs-mip.fr (A. Laforge), sara.fleury@legos.obs-mip.fr (S. Fleury).

¹ J. Verley started this study during his Master degree of engineering internship in 2017. He disappeared while mountaineering in March 2018. This work is dedicated to him.

Following the approach of Peacock and Laxon (2004), several sea ice freeboard estimations have already been published (Kurtz et al., 2014, 2015, 2016, 2017, 2018). The freeboard is calculated from the difference of sea ice heights (floes) and the sea level heights measured in the fractures (leads).

One main limitation of this approach comes from the strong back-scatter variations between the leads and the floes, that can reach up to 50 dB. This phenomenon has several impacts: (i) the resolution of the instrument prevents the very sharp lead waveforms from being sampled correctly, (ii) these waveforms are not modeled by the usual physical retracers (MLE3, MLE4) and (iii) the strong energy returned by lead echoes induces parasitic effects on floe returning echoes.

To limit the lack of resolution and the parasitic echoes impacts, the ESA has implemented two essential SAR processing options: the zero-padding (ZP), which increases the waveform sampling and the Hamming Window filter (HW) which reduces parasite echoes due to the side lobe effects (Smith, 2018). Note that these 2 options are not applied in the official Sentinel-3 A and B products. Currently, most of sea ice height estimations are based on heuristic retracers (or threshold retracers). These retracers define the surface returning point as a fixed percentage of the maximum amplitude of the waveform (sea ice, TFMRA), or its center of gravity (ice-1, OCOG). They are easy to implement and are able to produce a solution in the case of complex waveforms.

Physical retracers aim to fit the waveforms using a surface back-scattering physical model. These models consider several parameters governing the back-scattering such as the main back-scattering horizon, the back-scatter, the roughness or the altimeter misalignment to fit the waveforms. Prior to this study, the only physical retracking approach has been proposed by Kurtz et al. (2014). The CS2wF (CryoSat-2 WaveForm Fitting method) retracker presented in this paper is based on the variation of the back-scattering coefficient (σ naught) with the angle of incidence and a least squares fitting approach.

The different methodologies (ZP, HW, retracker) lead to different height estimations. For instance, Sallila et al. (2018) show an approximate 1 m (~50%) mean difference on CS-2 published sea ice thickness solutions whereas a 0.1 m (10%) precision is required. Note that the disparities between various freeboard solutions is an important issue in order to provide consensual sea ice thickness solutions for modelers and climatologists (Stroeve and Notz, 2018).

The purpose of this work is to estimate the impacts of the various options on the retrieved freeboard. It has been performed in the context of the ESA Cryo-SeaNice project. It benefits from the ESA's Grid Processing On Demand (GPOD) computing center and its SARvatore processing chain (about ten options for configuring SAR altimetry processing, including ZP and HW are available) which provides SAMOSA+ physical retracking solution (Dinardo et al., 2018). In this study, we investigate one empirical

retracer, the Threshold First Maximum Retracker Algorithm (TFMRA) (Helm et al., 2014) and the SAMOSA+ physical retracker (Sar Altimetry MOde Studies and Applications over ocean) (Dinardo et al., 2018), one of the only physical retracker available for sea ice surfaces. It is important to note that this work is the first assessment of SAMOSA+ over sea-ice surface. In addition, this paper challenges the use of the Hamming Window by introducing an alternative method to eliminate azimuthal ambiguities.

Using the ESA Grid Processing On Demand (GPOD) SARvatore chain on GPOD service (Dinardo et al., 2014), we compute four Cryosat-2 freeboard solutions over the period 2013–2017. All these solutions include zero-padding and they only differ by the retracking method (TFMRA or SAMOSA+) and the activation or not of the Hamming Window (HW). This approach enables to calculate the different solutions from the same source of data (ESA FBR) and through the same freeboard processing chain. Only the processing options differ. Using this methodology we evaluate separately the impacts on the heights of floes and the heights of leads. Compared to other studies, which only compare the impact on the freeboard, this approach is quite original. To assess the consistency of our results, we also investigate the data of the Copernicus Sentinel-3A mission (2016-), which carries an altimeter similar to that of CryoSat-2. Our results will also question the relevancy of using fixed leading edge thresholds for empirical retracers. Finally, the different solutions are compared with independent *in situ* measurements: the Operation Ice Bridge (OIB) airborne measurements and the Beaufort Gyre Exploration Project (BGEP) upward looking sonar measurements over the period 2013–2017.

The paper is structured as follow: Section 2 details the difficulties inherent to the freeboard measurement and presents the associated technical solutions. Section 3 presents the four freeboard solutions investigated in this paper. These solutions are analyzed in Section 4 and compared with *in situ* measurements in Section 5. Section 6 proposes with a correction for TFMRA calibrated on the physics of SAMOSA+.

2. Overview of the difficulties and technical solutions

2.1. Bandwidth limited resolution

The delay/Doppler altimeter uses pulse compression in the range dimension to combine an improved radial resolution with a low power pulse (Raney, 1998). The Range resolution R is constrained by the bandwidth B as described in Eq. (1):

$$\delta R = \frac{c}{2B} \quad (1)$$

where c is the speed of light in vacuum. The bandwidth reception of 320 MHz of SIRAL (and SRAL) aims to a range resolution of approximately 0.47 m (gate width). With this nominal vertical resolution, diffusive sea ice floes

surfaces are correctly sampled. Note that the large amount of floes tends to statistically counterbalance errors. On the contrary, leads are sparse, and their peaky waveform echoes are poorly sampled with the nominal range resolution of the instrument. This can induce important errors in sea surface height (SSH) interpolations between leads (Tilling et al., 2018; Lawrence et al., 2018). Errors on the SSH can be limited by over-sampling the waveforms by applying an order 2 zero-padding. This method extends the waveform length by a factor 2 prior to the range compression in the delay-Doppler processing. Note that, an order 2 zero-padding is systematically applied to the CryoSat-2 ice products distributed by ESA. It is not the case for the official Sentinel 3A & 3B data which explain the difficulties to retrieve sea ice freeboard with these products.

2.2. Retracking of non Brown-like waveform

The strong back-scatter over leads generates echoes that do not fit with the model proposed by Brown (1977) over the open ocean (Landy et al., 2019). Classical heuristic retrackerers such as ice-1 or sea-ice cannot be used either as they could get trapped by the numerous off-nadir or side-lobe effects induced by the nearby specular leads. We investigate here two retrackerers that can handle the peaky waveforms and the side-lobe effects: (1) the TFMRA, one of the most commonly used heuristic retracker over sea ice (Hendricks et al., 2016), and (2) SAMOSA+, a physical model based retracker mainly used for coastal oceanography.

TFMRA, presented in Helm et al. (2014) and in Quartly et al. (2019) for sea-ice applications, is derived from the heuristic retracker ice-1 (Bamber, 1994). This approach has the advantage to be easy to implement, computer efficient and robust on all types of surfaces. The main question addressed in this study is related to the impact of the fixed threshold, whereas the physical models have demonstrated that this threshold depends on several characteristics of the surface, and in particular its roughness.

SAMOSA+ (Dinardo et al., 2018) is based on the delay-Doppler analytical model SAMOSA2 described in Ray et al. (2015). The fitting scheme uses a constrained Levenberg-Marquardt Least Squares Estimation Algorithm to estimate three physical parameters: the epoch (τ_0), the significant wave height (SWH) and the amplitude (P_u). One of the major contributions of SAMOSA+ is its ability to model peaky waveforms over specular surfaces with a fourth parameter: the Mean Square Slope of the surface which parametrize secondary-scale surface roughness. For that purpose, SAMOSA+ classifies the echoes into two categories: diffusive and non-contaminated echoes in category 1 and all the others in category 2. At a first step, all echoes are fitted according to SAMOSA2 with the three physical parameters. Echoes of the second category are thereafter fitted using the Mean Square Slope (MSS) instead of the SWH as the third degree of freedom. One

objective of this study is to assess improvements coming from SAMOSA+ compared to empirical retrackerers.

2.3. Azimuth ambiguity (side-lobe effect)

2.3.1. Description

The azimuthal ambiguity, or side-lobe effect, is specific to the SAR mode. It only appears over complex surfaces such as sea-ice (Quartly et al., 2019). It is the result of low gain side-lobes surrounding the synthetic antenna beam main lobe. On most surfaces its impact is insignificant. Over sea ice, the altimeter successively measures diffuse ice floes and specular leads with strong back-scattering contrasts that can reach up to 50 dB. When the synthetic antenna main lobe measures at slant-view angle a diffusive floe, the low gain of synthetic side-lobes can be counterbalanced by the strong back-scattering power of a lead located at the nadir (see Fig. 1(a)). After the stacking and the azimuth integration of the 2D-stack (so called “multi-looking”), these side-lobe “ghost” contributions can be detected on the waveform before the nadir peak (Fig. 1(b)). By construction, this phenomenon can only affect the low back-scattering power encountered over floes. It can induce several meters of errors on the range estimation.

2.3.2. Filtering methods

The most common solution to filter this parasite effect is the Hamming Window (HW). The method consists in applying a cosine arch window function in the azimuth direction prior to the Fast Fourier Transform. This has the effect of attenuating the contributions of the side-lobe relatively to the main lobe. In counter part it creates a dilatation of about 30% of the PTR main lobe that lightly degrades the along-track resolution (see (Smith, 2018) for more details).²

To avoid this side effect, we have developed an alternative solution: the Side-Lobe Envelop Detection (SLD) method. Unlike the Hamming, this method does not impact the waveform. It consists in detecting and isolating waveform sequences impacted by side-lobes parasite peaks. The principle relies on the particularity that, over flat surfaces, side-lobe parasite peaks draw a parabolic shape on the along-track successive waveform representation (see Fig. 2(a)). Knowing that the side lobe effect can only occur on a Doppler beam slant-view angle while the satellite is at the vertical of a lead (cf. Fig. 1(a)), then the range r_i between the altimeter and the measured Doppler band T_i can be written as:

$$r_i^2 = Alt^2 + d_i^2 \quad (2)$$

where Alt is the distance between the altimeter and the lead at its nadir, and d_i is the ground distance separating the

² Another filtering method to reduce the side-lobe effects are under investigation (Smith, 2018). They should be soon available on GPOD for testing.

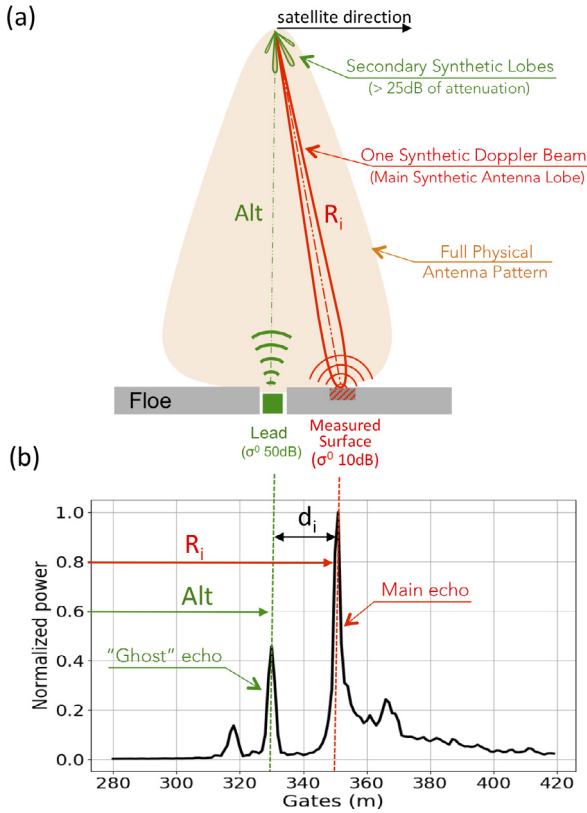


Fig. 1. Diagram to illustrate the side lobe effect over sea-ice: The SAR processing allows to focus on a limited part of the scene illuminated by the radar, typically a 300 m width stripe (in red, with the range R_i). The final waveform is elaborated from successive views R_i of this stripe. If a lead is nearby the measured strip, for some of these views (according to the width of the lead) the satellite will be at the nadir of the lead, as illustrated here. By construction of a synthetic Doppler antenna, the main lobe is always accompanied by lateral side lobes (in green on top). Their gains being very attenuated, they are generally not annoying, unless they are in the direction of a surface much more specular than the target strip, like a lead. The distance Alt between the altimeter and the lead being less than the distance R_i from the target, it results in a phantom peak in front of the main peak on the final waveform (b). (For interpretation of the references to colour in this figure legend, the reader is referred to the web version of this article.)

measured Doppler band T_i and the closest lead T_L (see Fig. 1(a)).

This distance d_i can be expressed as $N_{bands} \times \Delta x_{dop}$, where Δx_{dop} is the Doppler beam width (which only depends on the satellite altitude as explained in Raney (1998)) and N_{bands} is the number of Doppler bands separating the measured Doppler band T_i and the closest lead T_L . The range difference between Doppler bands T_i and T_L can be written:

$$\Delta r_i = r_i - r_L = r_i - Alt \quad (3)$$

From (2) and (3) we derive the following parabolic equation:

$$\Delta r_i^2 + 2h\Delta r_i - d_i = 0 \quad (4)$$

$$\Delta r_i = -Alt \left(1 \pm \frac{\sqrt{1 + d_i^2}}{Alt^2} \right) \quad (5)$$

Considering that d_i is much smaller than the satellite altitude Alt , the following approximation is done:

$$\Delta r_i \approx \frac{d_i^2}{2Alt} \quad (6)$$

This equation demonstrates that the side lobe peak trajectory follows a half parabolic line as a function of the distance d_i between the parasitic lead position (top of the parabola) and the considered Doppler beam (in the interval $[0, d_i]$).

Thus from each measurement classified as a lead, we compute the trajectory of the side lobes in the successive waveforms on both sides of the lead. This trajectory delimits a region outside which the measurements are not valid peaks (red parabola in Fig. 2).

According to the processing chain, this information can be used either to constraint the retracker to find out a solution within the region, or a posteriori to reject the retracker solutions that are outside the region.

This methodology is sensitive to the performance of the lead/floe classification, but it has the advantage of not altering the waveforms. In this study, the SLD algorithm is used to evaluate the impacts of the Hamming Window on freeboard estimations. This filter is implemented on the GPOD processing platform as an alternative to the Hamming window.

2.4. Across-track ambiguity (off-nadir effect)

2.4.1. Description

The off-nadir effect, or across-track ambiguity, is a well known effect as it also occurs with the traditional LRM mode (see for instance (Armitage and Davidson, 2013)). It occurs when across-track specular surfaces contaminate the waveform with additional peaks, which, unlike the case of side-lobes, appear after the nadir peak. To illustrate this effect, Fig. 3(b) shows an example of a Sentinel-2A image together with a concomitant CryoSat-2 track. The red circle shows an across-track gate affected by the presence of a nearby lead. Although the across-track ambiguity is reduced in SAR mode, it is still responsible for substantial retracking errors. The across-track ambiguity is easily distinguishable from side-lobe retracking errors since it underestimates heights while side lobe effect overestimates heights.

2.4.2. Filtering method

An off-nadir effect is easier to detect than a side-lobe effect as the parasitic peak is always behind the peak that corresponds to the nadir. We have developed a First Peak Detection Method (FPD), very similar to the one implemented in TFMRA, to detect the first peak and flag the

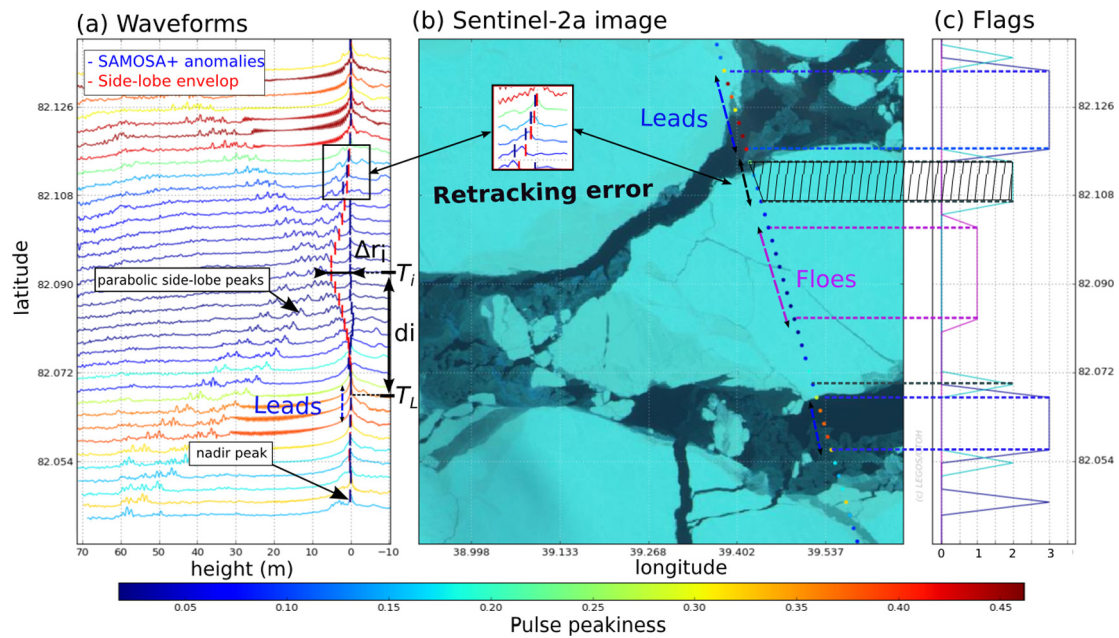


Fig. 2. Summary diagram of the principle of the **Side-Lobe Envelop Detection method (SLD)**. (a) is the along-track waveforms corresponding to (b) a CS2 track concomitant a Sentinel-2a image. (c) plots the corresponding leads (dark blue), floes (purple), retracking errors (light blue). The flags are 1 for floes, 2 for filtered floes and 3 for leads. On (a) the side-lobe envelop defined by Δr_i (Eq. (6)) and the SAMOSA+ height anomalies are displayed on the waveforms. The zoomed area shows an example of side-lobe induced retracking errors detected by the SLD method. (For interpretation of the references to colour in this figure legend, the reader is referred to the web version of this article.)

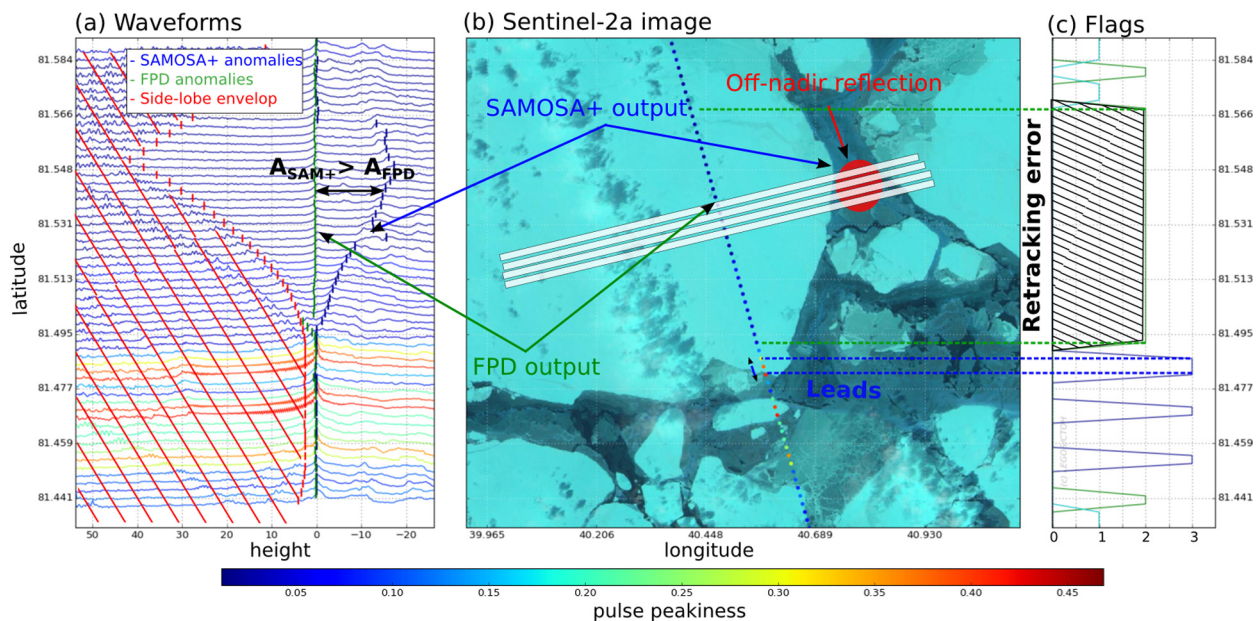


Fig. 3. Summary diagram of the **First peak detection method (FPD)**. (a) represents the along-track waveforms corresponding to (b) a CS2 track concomitant to a Sentinel-2A image. (d) plots the corresponding detected leads (in dark blue), floes (in purple) and retracking errors due to off-nadir returns (in light blue). The flags are 1 for floes, 2 for filtered floes and 3 for leads. On waveforms (a) are displayed in red the side-lobe envelopes defined in Fig. 2, in green the low threshold FPD height anomalies and in blue the SAMOSA+ height anomalies. (For interpretation of the references to colour in this figure legend, the reader is referred to the web version of this article.)

peaks that fall behind the gate of this first. The Side-Lobe Detection (SLD) precedes this operation in order to first filter potential side-lobe peaks.

In the example Fig. 3, the side-lobe envelope is indicated in red-hatched line, the first peak height anomalies are in

green and the SAMOSA+ height anomalies are in blue. Off-nadir retracking errors are shown in black-hatched line in 3(c). Using SAMOSA+, about 10–15% of the data are filtered, which demonstrates its sensitivity to off-nadir contamination.

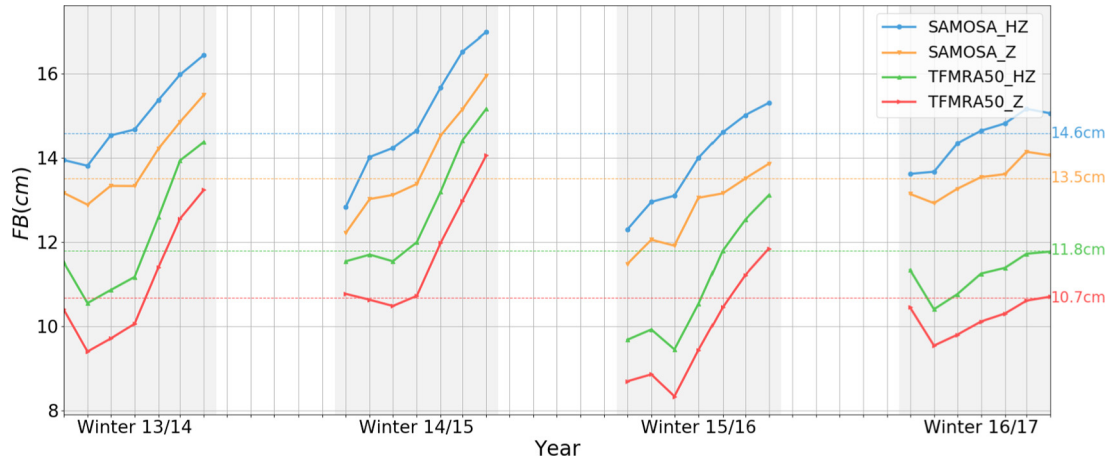


Fig. 4. Temporal series of mean freeboard for four freeboard solutions (TFMRA50_Z, TFMRA50_HZ, SAMOSA_Z, SAMOSA_HZ). The mean freeboard is computed over a common mask to all solutions for each month.

3. Algorithm and freeboard solutions

The previous section described the main difficulties inherent to the SAR mode freeboard estimation and solutions to get around them. Here, we analyse the effects on the freeboard of these various solutions. For that purpose, we have computed four radar freeboard data-sets presented in Table 1.

The Fig. 5 gives an overview of the processing chain used to produce the freeboard data-sets. Level L1B and L2 data are processed in the GPOD processing cluster. Among all the processing options offered by the SARvatore interface, only two combinations are used in this study: the zero-padding only (noted Z) or the zero-padding combined with the Hamming Window (noted HZ). The ranges output by the retracker are converted into surface height anomaly by applying the oceanic and atmospheric corrections (Quartly et al., 2019) referenced against the mean sea surface MSS_DTU15 provided by the Technical University of Denmark (DTU) in 2015. We use the Pulse Peakiness (PP) criteria to classify the floes and the leads as introduced by Giles et al. (2008) and Peacock and Laxon (2004). Waveforms with PP values over 0.3 are considered as leads and waveforms with PP below 0.1 are considered as floes (these values are for zero-padded waveforms). The echoes with PP between these 2 values are discarded. From this classification, we compute surface height anomalies for both sea ice and ocean: the Ice Surface Anomaly (ISA) and the Sea Surface

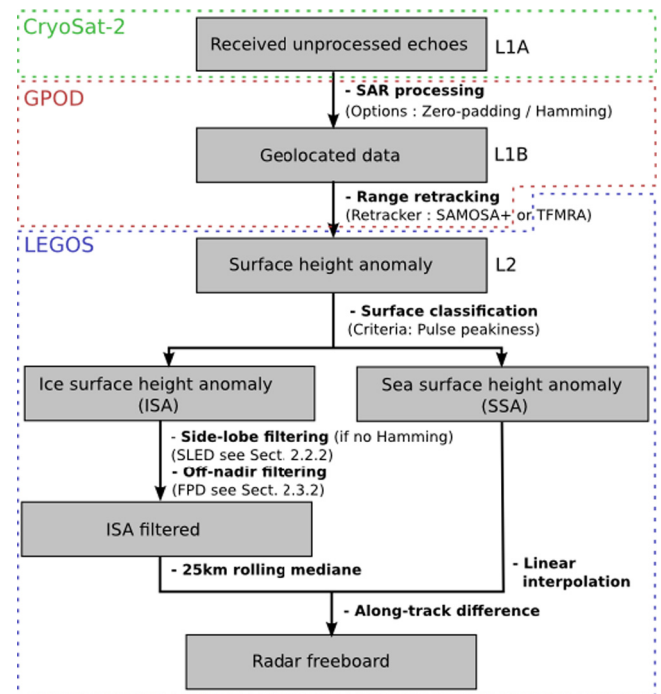


Fig. 5. Flowchart of the LEGOS radar freeboard processing algorithm.

Anomaly (SSA). The SLD methodology and the FPD methodology are applied to the sea ice surface height anomalies in order to only keep relevant estimations. A 25 km rolling median is applied on the ice (ISA) and ocean (SSA) surface anomalies to smooth the data. In case of successive SSA measurements within a same lead, we retain the median of these measurements as the SSA of the lead. Sea level anomalies under floes are calculated from a linear interpolation between the SSA of the leads. Finally, the along-track radar freeboard is computed from the differences of the interpolated ISA and SSA.

Using this algorithm four freeboard products are generated following the procedures:

Table 1
Freeboard solution to be evaluated in this study.

Retracker	Side-lobe filtering	
	SLD	Hamming
TFMRA	TFMRA50_Z	TFMRA50_HZ
SAMOSAS+	SAM_Z	SAM_HZ

- The zero-padding is always activated.
- The off-nadir peaks are filtered with the First Peak Detection (FPD). Since FPD has no impact on the shape of the waveform, it is systematically activated.
- Either the Hamming filter or the SLD is activated to avoid the side-lobes. This will allow evaluating the effect of the Hamming on the ISA and SSA.
- Both the SAMOSA+ and the TFMRA retrackerers are computed for comparison purpose.

The pan-Arctic mean radar freeboard time series of the four output products are presented in Fig. 4 for the period 2013–2017. The along-track data are gridded for each month with an EASE-2 grid with 12.5 km resolution. A median smoothing filter with a radius of 25 km is applied in order to statistically filter out outliers. Since all these freeboards are processed with the same algorithms, differences are only due to the retracker (SAMOSA+ or TFMRA50) or the side-lobe filtering methodology (Hamming or SLD.).

Fig. 4 shows that the differences do not depend on the period. The aim of the next sections is to explain these differences and to point out the most adapted solution.

4. Inter-comparison study

4.1. Comparison of the Hamming

4.1.1. Methodology

In this study, we separately compare the heights of the leads and the heights of the floes for each processing option: Hamming vs No Hamming (Section 4.1.2) and SAMOSA+ versus TFMRA50 (Section 4.2). Note that when the Hamming is deactivated, it is always substituted by the SLD method (see Section 2.3.2). Statistics are calculated on monthly average for March 2015 for CryoSat-2 and December 2016 for Sentinel-3A.

4.1.2. Hamming impact and analysis

Fig. 6 displays the CS-2 distributions of height differences between HZ and Z products over leads and floes for March 2015 for the 2 retracking methods. It shows that the TFMRA is strongly influenced by regional variations of surface roughness. Height differences induced by the Hamming window reach 5 cm in Multi Year Ice (MYI) regions and are close to zero in smooth marginal ice zones. This is due to the fact that the HW widens the leading edge of the waveform. This effect increases with the roughness of the surface and the flattening of the waveform, which increases the bias between HZ and Z. This detrimental effect is responsible for a notable mean bias of 2 cm for TFMRA50.

There are no such effects with SAMOSA+ as the physical approach takes into account roughness variations of the surface and the application of the HW in its model. A regional influence is still perceptible in marginal ice zone and North East of Greenland where -4 cm biases can be

locally reached. Indeed, along-track height anomaly comparisons between HZ and Z computed with SAMOSA+ show that HZ data are more sensitive to off-nadir errors than Z data in these thin ice fractured regions.

Over the leads, a global and regionally constant bias of 0.4 cm for TFMRA50, and of -1.9 cm for SAMOSA+ is found. The TFMRA small bias indicates that the shape of specular waveforms (over leads) is not impacted by the Hamming Window. This is an expected result as the side-lobe effect impacts only the lower back-scattering surfaces. Thus the -1.9 cm bias for SAMOSA+ cannot be explained other than by a problem with the implementation of the physical retracker when Hamming is enabled.³

The same studies performed with Sentinel 3-A data leads to similar conclusions. Mean biases are presented in Table 2.

The resulting impacts of the Hamming window on the mean freeboard for March 2015 are of 1.6 cm for TFMRA50 and 1.1 cm for SAMOSA+. The order of magnitude of these biases are in agreement with the mean freeboard differences presented in Fig. 4.

4.2. Comparison of the retrackerers

Fig. 7(a) shows the freeboard differences between SAMOSA_Z and TFMRA50_Z for the period 2013–2017. The mean difference for pan-Arctic sea ice is 1.3 cm. When separating the FYI and the MYI (using OSI-SAF sea ice type product), a mean difference of respectively $+4.2$ cm and -2.6 cm can be found. This disparity, depending on the ice type, is illustrated in Fig. 7 (b). Fig. 7(c) represents the trend of the mean freeboard difference between SAMOSA+ and TFMRA50 function of the mean PP for each pixel. It shows that the mean freeboard difference increases as roughness decreases, meaning that the TFMRA50 over-estimates rough ice and under-estimates smooth ice relatively to SAMOSA+. This is consistent with the correlation between freeboard and roughness observed in Fig. 7 and with the results presented in Landy et al. (2019)⁴. This figure illustrates the errors induced by the variability of surface roughness when using a fixed threshold.

5. In-situ comparisons

In this section, we compare the freeboards solutions with *in situ* measurements. Two types of independent

³ This problem has been reported and solved in the new versions of GPOD (>v2.25). It came from the fact that SAMOSA+ previous Doppler beam width correction when Hamming was activated was the same over open ocean and the over the leads, which was a wrong hypothesis.

⁴ SAMOSA+ uses a Gaussian surface height probability density function (PDF) to represent the surface roughness distribution. Landy et al. (2019) argues that a log-normal distribution of the sea ice surface would be better than the Gaussian distribution used with SAMOSA+. This should need further investigations.

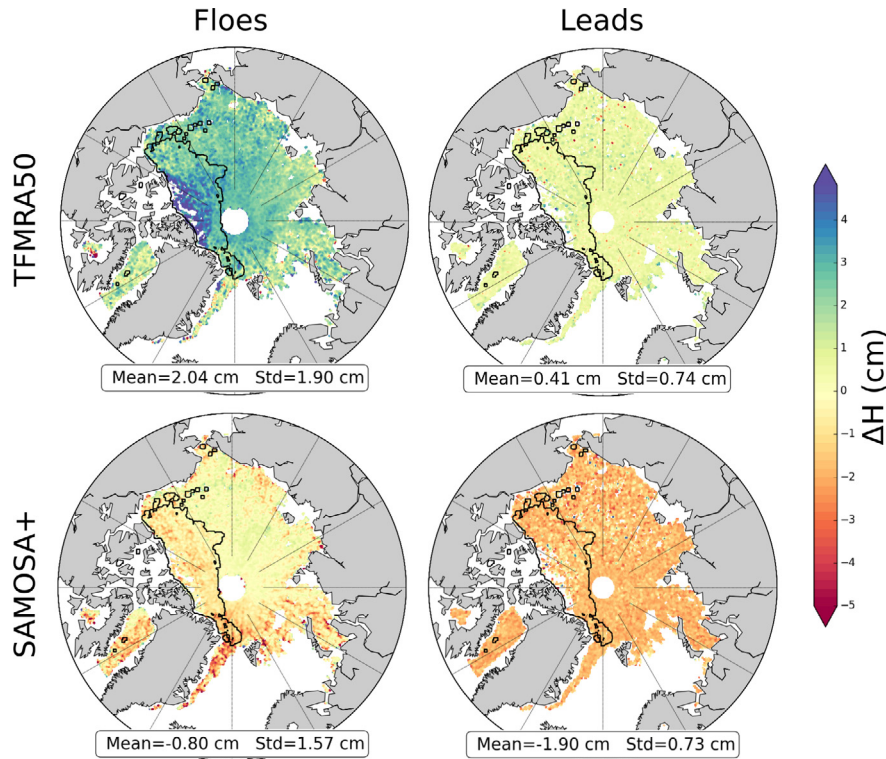


Fig. 6. Effet of the Hamming on floe heights (left column) and lead heights (right column) according to the retracker: the maps display the differences HZ-Z for March 2015. When the hamming is not applied it is replaced by the SLD filter. The black line delimits Multi Year Ice (MYI) and First Year Ice (FYI) from the mid-March 2015 OSI-SAF ice-type products.

Table 2

Summary table of the impacts of the Hamming window on the height measured over leads and floes for TFMRA and SAMOSA+ (columns) and for CryoSat-2 and Sentinel-3 (lines). Differences between ΔH_{floes} and ΔH_{leads} provide an estimation of the corresponding mean freeboard differences.

cm	TFMRA		SAMOSA+	
	$\Delta H_{floes} - \Delta H_{leads}$	ΔFB	$\Delta H_{floes} - \Delta H_{leads}$	ΔFB
$Fb_{HZ} - Fb_Z$				
$\Delta FB_{c2Sgpod}$	2.0(-0.4)	1.6	-0.8(-1.9)	1.1
ΔFB_{s3gpod}	1.8(-0.5)	1.3	-0.1(-1.4)	1.5

in situ data are considered. The first data set is from the NASA Operation Ice Bridge (OIB) mission, which covers a large area in the West Arctic with airborne altimeters. The second data set comes from the Beaufort Gyre Exploration Project (BGEF), which provides ice draft measurements from under water moorings.

5.1. Operation Ice Bridge data B

Operation Ice Bridge, or OIB is an airborne NASA survey operating in Arctic since 2009, usually from mid-March to mid April (Kurtz et al., 2012). The aircraft is equipped with an ATM laser radar measuring the total freeboard (ice freeboard + snow cover) and a snow radar to measure snow depth. Depending on the lead density, the uncertainties on the total freeboard vary from 1 cm

to 30 cm (Kurtz et al., 2012). The uncertainty for the snow depth is about 5.7 cm (Kurtz and Farrell, 2011). The sea ice freeboard (FB) is calculated from the difference between the total laser freeboard (FBT) and the snow depth (SD) of the snow radar.

$$FB = FBT - SD \tag{7}$$

This ice freeboard FB cannot be directly compared with the radar freeboard FB_{Ku} measured with CryoSat-2 or Sentinel-3 because of the reduction of the Ku wave speed propagation in the snow layer. It must be first converted to a “radar like” freeboard using the formulation suggested by Giles et al. (2008):

$$FB_{Ku} = FB - (1 - \alpha)SD \tag{8}$$

where α represents the Ku-wave celerity ratio in the snow layer (Ulaby et al., 1986):

$$\alpha = \frac{c_s}{c} = (1 + 0.51\rho_s)^{-1.5} \tag{9}$$

Except for the late April/May 2016 campaign (because of the presence of melt-ponds that perturbs the lead/floe classification), all OIB campaigns from 2013 to 2017 have been considered in this study. The OIB tracks are gridded on EASE2 grid with a 12.5 km pixel resolution similar to the one used for CryoSat-2 data. As illustrated Fig. 8 the smaller bias and RMSD are obtained with the SAMOSA+, Z solution.

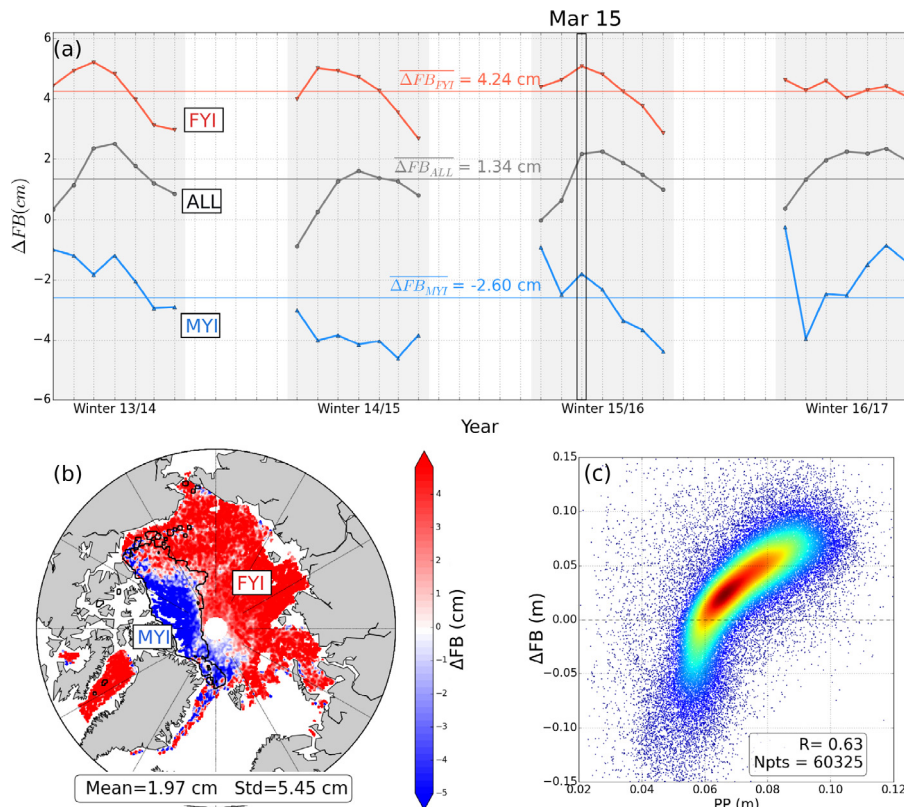


Fig. 7. (a) is the temporal series of the mean freeboard differences between the SAMOSA_Z and TFMRA50_Z solutions over FYI (red), MYI (blue) and pan-Arctic (grey) for the period 2013–2017. (b) is a map of these freeboard differences for March 2015. The black line in b mark the limit between Multi Year Ice (MYI) and First Year Ice (FYI) from mid-March 2015 OSI-SAF ice type data. (c) is the freeboard differences of (a) as a function of the waveform Pulse Peakiness (PP). (For interpretation of the references to colour in this figure legend, the reader is referred to the web version of this article.)

5.2. Beaufort Gyre Exploration project data

The Beaufort Gyre Exploration Project (BGEP) is composed of 3 or 4 Upward Looking Sonars moored in the Beaufort Sea (<http://www.who.edu>, (Melling et al., 1995)). Every half second, these sonars provide measurements of the distance to the bottom of the sea ice thereafter converted to ice draft with an accuracy of about 5 cm.

The conversion from “radar” freeboard to ice draft is based on the hydrostatic equilibrium equation:

$$SIT = \frac{\rho_w}{\rho_w - \rho_i} FB_{Ku} + \frac{(1 - \alpha)\rho_w + \rho_s}{\rho_w - \rho_i} SD \quad (10)$$

where ρ_w , ρ_i and ρ_s are the respective density of seawater, ice and snow. The sea water density is set to 1024 kg m^{-3} . Alexandrov et al. (2010) suggest to use a MYI density of 882 kg m^{-3} and of 917 kg m^{-3} for the FYI. To be consistent with OIB the snow density is set to 320 kg m^{-3} . The snow depth (SD) data come from Saral/CS-2 Ka/Ku bi-frequency measurements (Guerreiro et al., 2016). The draft is calculated by subtracting the freeboard from the ice thickness:

$$Draft = SIT - FB_{Ku} \quad (11)$$

This “altimetric” draft is monthly averaged within a 20 km radius centered on each mooring position and compared for all freeboard products over the entire 2013–2017 period (Fig. 9).

5.2.1. Comparative results with in situ data

Results of the comparisons are gathered in Table 3. Additional results, issued from a comparison with TFMRA 60% (Guerreiro et al., 2017), are also presented.

The SAMOSA_Z solution provides the lower biases ($Bias_{OIB} = 0.13 \text{ cm}$ / $Bias_{BGEP} = 13 \text{ cm}$) and root mean square deviations ($RMSD_{OIB} = 7 \text{ cm}$ / $RMSD_{BGEP} = 36 \text{ cm}$). These biases are consistent with observations over the entire Arctic from Section 4 where we observed a 1.6 cm bias over leads.

The larger root mean square deviations for TFMRA is an effect of the fixed threshold. The differences between TFMRA_50 and TFMRA_60 illustrates the sensitivity of the choice of the threshold value. The effect of the Hamming also depends on the choice of the threshold. As demonstrated in Section 4.1.2, this effect is caused by the widening of the waveform leading edge over the floes.

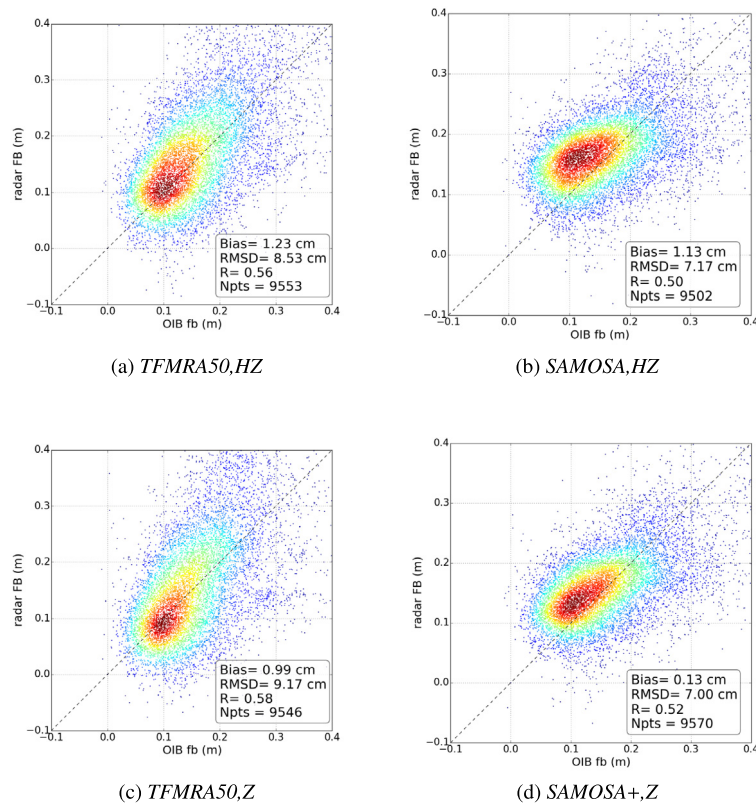


Fig. 8. Comparison between Ice Bridge and four CS2 freeboard solutions (a) TFMRA_Z, (b) TFMRA_HZ, (c) SAMOSA_Z, (d) SAMOSA_HZ on four campaigns (2013, 2014, 2015, 2017).

Because this effect does not occur over the leads, it is not compensated while computing the heights differences.

5.2.2. Discussion

These *in situ* comparisons comfort the advantage of the physical retracker relatively to the heuristic approaches. However, all the comparisons with *in situ* data involve a tiers parameter that is not well known: snow depth. The uncertainties on this parameter can have significant impacts on the validations. Five options exist to take into account snow depth: OIB snow radar measurements (Kurtz and Farrell, 2011), dual band Ka/Ku height comparisons (Guerreiro et al., 2016; Lawrence et al., 2018), Passive Microwave Radiometers measurements (Rostosky et al., 2018), the Warren Climatology (Warren et al., 1999) and climate reanalysis models (Petty et al., 2018). In our comparisons two independent snow depth observations have been considered: OIB snow radar measurements (Kurtz and Farrell, 2011), and the Alti Snow Depth from Ka/Ku height comparisons (Guerreiro et al., 2016) for the validation against BGEP. They are clearly much more reliable than the usual Warren99 climatology but some complementary studies on snow depth observation would be required to improve the validations against *in situ* data. The confidence on the presented results mainly rely on the independence between the BGEP and Operation Ice Bridge derived radar freeboard measurements.

6. Roughness correction for threshold retracker

The results presented in this article demonstrate that SAMOSA+ provides better results than the TFMRA. As already explained, the main limitation of heuristic retracker is the use of a constant threshold, independently to the surface roughness. The impact is illustrated in Fig. 7(c) which shows the freeboard differences between SAMOSA+ and TFMRA50 according to the Pulse Peakiness.

These differences between SAMOSA+ and TFMRA can be used as a correction function in order to correct TFMRA from the roughness variations over the floes.

An alternative option would be to adapt the TFMRA threshold according to the Pulse Peakiness. But this would aim to thresholds close to the maximum and induce larger dispersions (RMSD). Indeed, because of the sampling, the maximum of the waveform can not be retrieved with a precision better than half a gate, which would reduced the interest of the retracker. In contrary, the epoch is much more stable against the variability of the sampling positions when the threshold hits the steepest slope of the leading edge.

The lower curve of Fig. 10(a) shows that the threshold that optimises the RMSD is about 30%. We have nevertheless chosen a threshold of 50% because it is largely used in the literature, the RMSD remains reasonable and it limits

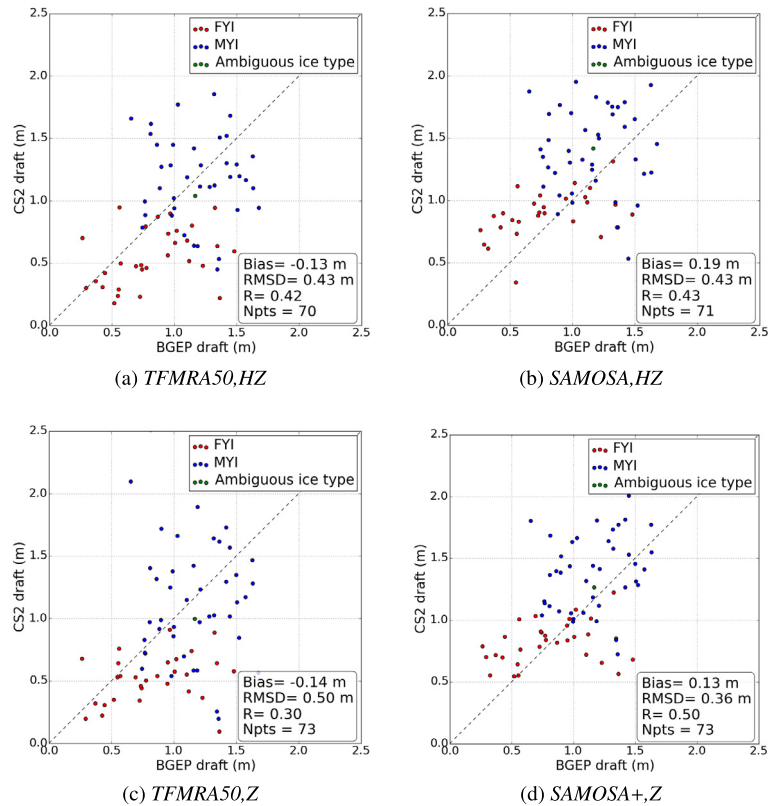


Fig. 9. Comparison between the Beaufort Gyre Exploration Project (BGEP) and four CS2 freeboard solutions (a) TFMRA_Z, (b) TFMRA_HZ, (c) SAMOSA_Z, (d) SAMOSA_HZ over four winters 2013 to 2017.

Table 3

Summary table of the *in situ* comparisons for 6 freeboard solutions TFMRA60_HZ, TFMRA60_Z, TFMRA50_HZ, TFMRA50_Z, SAM_Z, SAM_HZ.

$H_{CS2} - H_{in-situ}$ (cm)		OIB freeboard (mean ~ 15 cm)			BGEP draft (mean ~ 100 cm)		
		Bias	RMSD	R	Bias	RMSD	R
TFMRA60	HZ	-2.8	8.8	0.56	-32	49	0.38
	Z	-3.9	9.0	0.57	-39	53	0.41
TFMRA50	HZ	1.2	8.5	0.56	-13	43	0.42
	Z	1.0	9.2	0.58	-14	50	0.30
SAMOSAS+	HZ	1.1	7.2	0.50	19	43	0.43
	Z	0.1	7.0	0.52	13	36	0.50

the risk to be trapped by noises in front of the main leading edge. As shown in the top curve of Fig. 10(a), the lower is the threshold, the higher is the bias on the epoch that must be corrected. Our objective is to correct this bias. It is also important to recall that this bias is partly compensated during the freeboard calculation as it is the difference between two ranges. Fig. 7 (b) presents the correction function that should be applied over the floes while using TFMRA50 to account for the roughness.

The black dotted line is an order 3 polynomial fitting which provides an acceptable root mean square deviation of 0.85 cm. Finally, we recommend to apply the following range corrections on the ranges output from TFMRA50_HZ. This correction $corr$, in meters, only depends on the pulse peakiness pp :

$$corr = \begin{cases} -1390pp^3 + 339pp^2 - 28.4pp + 0.994 & pp < 0.1 \\ 0.25 & pp > 0.33 \end{cases} \quad (12)$$

The case $pp < 0.1$ corresponds to the floes and the case $pp > 0.33$ corresponds to the leads. The data in-between are considered ambiguous.

These corrections must be applied on the TFMRA50_HZ ranges over leads and floes prior the freeboard computation. The improvements are demonstrated by comparisons with OIB and BGEP. The Table 4 shows that this correction allows to decrease the RMSD against OIB from 9.2 cm to 7.4 cm and from 50 cm to 34 cm against BGEP:

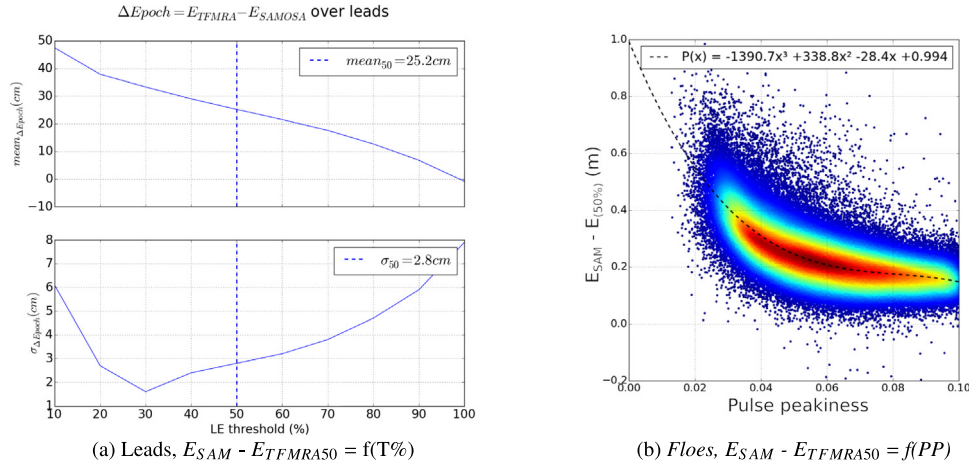


Fig. 10. Range differences between SAMOSA+ and TFMRA: (a) shows the mean differences over leads as a function of the threshold (T%). (b) is the epoch difference between SAMOSA and the TFMRA 50% as a function of the pulse peakiness. The cloud of point is fitted with a order 3 polynomial function (RMSD = 0.85 cm).

Table 4

Summary table of the *in situ* comparisons for 3 freeboard solutions TFMRA50_Z, SAM_Z, TFMRA50_HZcorr

$H_{CS2} - H_{in-situ}$ (cm)		OIB freeboard (mean 15 cm)			BGEP draft (mean 100 cm)		
		Bias	RMSD	R	Bias	RMSD	R
TFMRA50	Z	1.0	9.2	0.58	-14	50	0.30
SAM+	Z	0.1	7.0	0.52	13	36	0.50
TFMRA50corr	HZ	-0.7	7.4	0.56	-4	34	0.46

this solution could help to improve TFMRA outputs when no physical retracker is available.

7. Conclusion

In this paper, we have analyzed the effect of the Hamming and the performance of the physical retracker SAMOSA+ compare to the empirical TFMRA retracker. For this purpose, we inter-compared four freeboard solutions issued from the GPOD SARvatore service (<https://gpod.eo.esa.int/>). These solutions were thereafter compared with independent airborne and mooring *in situ* measurements. Globally, the comparisons with *in situ* measurements show that the SAMOSA+ physical retracker provides lower biases and RMSD.

The Hamming window induces biases for both retrackerers. As it tends to enlarge the waveforms, this effect was expected for the threshold retracker but not for the physical retracker. For the TFMRA this effect is more important for the multi-year ice (5 cm) than for the first-year ice. This must be taken into account. One alternative solution is to use the Side Lobe Detection (SLD) filter (presented in this paper) instead of the Hamming filter. Regarding SAMOSA+, the Hamming Window filter only impacts the leads. This issue has been reported to the GPOD team. Preliminary tests with the last SARvatore version (previous to v2.26) show that this problem can be solved. In general, this filter is not necessary with SAMOSA+ and should be avoided

for versions older than v2.26. For this new version, the Hamming should not impact the range retrieval. However, side lobe effects remain an issue for SAMOSA+. We therefore recommend to use the SLD to detect and reject these cases. Similarly, SAMOSA+ sometimes selects off-nadir peaks instead of first nadir peaks. This problem can be solved using the First Peak Detection (FPD). Note that both the SLD and the FPD have been implemented in GPOD and are currently under evaluation.

While physical retrackerers increase the accuracy of height measurements, they are much more complex to implement. In order to reach the level of accuracy of physical retrackerers with an empirical approach we have elaborated a correction function depending on the deviations between SAMOSA+ and the TFMRA relatively to the Pulse Peakiness, a proxy of the surface roughness. It can be easily computed with a TFMRA50 retracker. Relatively to *in situ* data, we have shown that this correction reduces the biases (0.3 cm for OIB and 10 cm for BGEP) and the RMSD (1.8 cm for OIB and 16 cm for BGEP).

Finally, we propose the following recommendations for future freeboard and sea level anomaly estimation over sea ice surfaces:

- The zero-padding is mandatory to retrieve the sea level (in leads).
- The physical retracker provide much more accurate measurements.

- Side lobes must be filtered using either a Hamming filter (or a similar approach) or the side lobe detection (SLD) filter presented in this paper. The SLD can be used prior to the retracking or a posteriori to remove unexpected low ranges.
- Off-nadir peaks must be filtered out using the First Maximum Detection (FMD). The FMD is already implemented in the TFMRA retracker.
- A threshold retracker can replace the physical approach as long as a correction function to account for the threshold variability according to the surface roughness is applied. Such a correction is provided in this paper. Note that it is only valid using a TFMRA50_HZ retracking configuration.

The results of this paper suggest that the best solution is obtained with the SAMOSA+ \underline{Z} configuration with the SLD and the FPD filters. This solution has been computed during all Arctic winters (October to April) over the period 2010–2019 (with SAR/SARIN modes). This data-set is available on request on <http://ctoh.legos.obs-mip.fr/data/sea-ice-products>.

This study confirms the recommendations expressed during the CryoSat-2 Scientific Expert Meeting held at ESA/ESRIN on 07–08 November 2017 (<https://earth.esa.int/documents/10174/1822995/CryoSat-CSEM-Summary-and-Recommendations-Report.pdf>). It should help to define future ESA CryoSat-2 sea-ice products, including improved geophysical parameters associated with quality index.

Finally, the SAMOSA+ sea ice freeboard solutions presented in this paper increase our confidence to move towards accurate multi-surface physical retrackers in the near future.

Acknowledgment

This work has been funded by the ESA Cryo-SeaNice Project. All the SAMOSA+ data-sets presented in this paper have been computed with the SARvatore processing chain the ESA GPOD platform (<https://gpod.eo.esa.int/>). Close collaboration with the GPOD team has resulted in mutual progress that should benefit the entire community. We would like to thank them warmly, and especially Giovanni Sabatino who has very patiently responded to all our intensive requests. We also thanks the anonymous reviewers who have provided essential comments and guidelines to improve the content and the fluidity of this paper.

References

Alexandrov, V., Sandven, S., Wahlin, J., Johannessen, O., 2010. The relation between sea ice thickness and freeboard in the arctic. *The Cryosphere* 4, 373–380.

Armitage, T.W., Davidson, M.W., 2013. Using the interferometric capabilities of the esa cryosat-2 mission to improve the accuracy of sea ice freeboard retrievals. *IEEE Trans. Geosci. Remote Sens.* 52, 529–536.

Bamber, J., 1994. Ice sheet altimeter processing scheme. *Int. J. Remote Sens.* 15, 925–938.

Blockley, E.W., Peterson, K.A., 2018. Improving met office seasonal predictions of arctic sea ice using assimilation of cryosat-2 thickness. *The Cryosphere* 12, 3419–3438. <https://doi.org/10.5194/tc-12-3419-2018>.

Brown, G., 1977. The average impulse response of a rough surface and its applications. *IEEE Trans. Antennas Propag.* 25, 67–74.

Dinardo, S., Fenoglio-Marc, L., Buchhaupt, C., Becker, M., Scharroo, R., Fernandes, M.J., Benveniste, J., 2018. Coastal sar and plrm altimetry in German bight and west baltic sea. *Adv. Space Res.* 62, 1371–1404.

Dinardo, S., Lucas, B., Benveniste, J., 2014. Sar altimetry processing on demand service for cryosat-2 at esa g-pod. In: Proc. of 2014 Conference on Big Data from Space (BiDS'14), p. 386. <https://doi.org/10.1016/j.asr.2017.12.018>.

Giles, K.A., Laxon, S.W., Ridout, A.L., 2008. Circumpolar thinning of arctic sea ice following the 2007 record ice extent minimum. *Geophys. Res. Lett.* 35, L22502. <https://doi.org/10.1029/2008GL035710>, URL: <https://agupubs.onlinelibrary.wiley.com/doi/abs/10.1029/2008GL035710>, arXiv:<https://agupubs.onlinelibrary.wiley.com/doi/pdf/10.1029/2008GL035710>.

Guerreiro, K., Fleury, S., Zakharova, E., Kouraev, A., Rémy, F., Maisongrande, P., 2017. Comparison of cryosat-2 and envisat radar freeboard over arctic sea ice: toward an improved envisat freeboard retrieval. *The Cryosphere* 11, 2059–2073.

Guerreiro, K., Fleury, S., Zakharova, E., Rémy, F., Kouraev, A., 2016. Potential for estimation of snow depth on arctic sea ice from cryosat-2 and saral/altika missions. *Remote Sens. Environ.* 186, 339–349.

Helm, V., Humbert, A., Miller, H., 2014. Elevation and elevation change of greenland and antarctica derived from cryosat-2. *The Cryosphere* 8, 1539–1559.

Hendricks, S., Ricker, R., Helm, V., 2016. User guide-awi cryosat-2 sea ice thickness data product v1, 2).

Kurtz, N., Farrell, S., Studinger, M., Galin, N., Harbeck, J., Lindsay, R., Onana, V., Panzer, B., Sonntag, J., 2012. Sea ice thickness, freeboard, and snow depth products from operation icebridge airborne data. *The Cryosphere Discussions* 6, 4771–4827.

Kurtz, N.T., Farrell, S.L., 2011. Large-scale surveys of snow depth on arctic sea ice from operation icebridge. *Geophys. Res. Lett.* 38, L20505. <https://doi.org/10.1029/2011GL049216>.

Kurtz, N.T., Galin, N., Studinger, M., 2014. An improved cryosat-2 sea ice freeboard retrieval algorithm through the use of waveform fitting. *The Cryosphere* 8, 1217–1237.

Kwok, R., Cunningham, G., 2015. Variability of arctic sea ice thickness and volume from cryosat-2. *Phil. Trans. R. Soc. A* 373, 20140157.

Landy, J.C., Tsamados, M., Scharien, R.K., 2019. A facet-based numerical model for simulating sar altimeter echoes from heterogeneous sea ice surfaces. *IEEE Trans. Geosci. Remote Sens.* 57, 4164–4180. <https://doi.org/10.1109/TGRS.2018.2889763>.

Lawrence, I.R., Tsamados, M.C., Stroeve, J.C., Armitage, T.W., Ridout, A.L., 2018. Estimating snow depth over arctic sea ice from calibrated dual-frequency radar freeboards. *The Cryosphere* 12, 3551–3564.

Melling, H., Johnston, P.H., Riedel, D.A., 1995. Measurements of the underside topography of sea ice by moored subsea sonar. *J. Atmos. Technol.* 12, 589–602.

Parrinello, T., Shepherd, A., Bouffard, J., Badessi, S., Casal, T., Davidson, M., Fornari, M., Maestroni, E., Scagliola, M., 2018. Cryosat: Esa ice mission—eight years in space. *Adv. Space Res.* 62, 1178–1190.

Peacock, N.R., Laxon, S.W., 2004. Sea surface height determination in the arctic ocean from ers altimetry. *J. Geophys. Res.: Oceans* 109, C07001. <https://doi.org/10.1029/2001JC001026>.

Petty, A.A., Webster, M., Boisvert, L., Markus, T., 2018. The nasa eulerian snow on sea ice model (nesosim) v1.0: initial model development and analysis. *Geoscient. Model Develop.* 11, 4577–4602. <https://doi.org/10.5194/gmd-11-4577-2018>.

Quarty, G.D., Rinne, E., Passaro, M., Andersen, O.B., Dinardo, S., Fleury, S., Guillot, A., Hendricks, S., Kurekin, A.A., Müller, F.L., et al., 2019. Retrieving sea level and freeboard in the arctic: a review of current radar altimetry methodologies and future perspectives. *Remote Sens.* 11, 881.

- Raney, R.K., 1998. The delay/doppler radar altimeter. *IEEE Trans. Geosci. Remote Sens.* 36, 1578–1588.
- Ray, C., Martin-Puig, C., Clarizia, M.P., Ruffini, G., Dinardo, S., Gommenginger, C., Benveniste, J., 2015. Sar altimeter backscattered waveform model. *IEEE Trans. Geosci. Remote Sens.* 53, 911–919.
- Rostosky, P., Spreen, G., Farrell, S.L., Frost, T., Heygster, G., Melsheimer, C., 2018. Snow depth retrieval on arctic sea ice from passive microwave radiometers improvements and extensions to multiyear ice using lower frequencies. *J. Geophys. Res.: Oceans* 123, 7120–7138.
- Sallila, H., McCurry, J., Farrell, S.L., Rinne, E., 2018. Assessment of contemporary satellite sea ice thickness products for arctic sea ice. *The Cryosphere Discussions* 2018, 1–44. <https://doi.org/10.5194/tc-2018-197>.
- Smith, W.H., 2018. Spectral windows for satellite radar altimeters. *Adv. Space Res.* 62, 1576–1588.
- Stroeve, J., Notz, D., 2018. Changing state of arctic sea ice across all seasons. *Environ. Res. Lett.* 13, 103001, URL: <http://stacks.iop.org/1748-9326/13/i=10/a=103001>.
- Tilling, R.L., Ridout, A., Shepherd, A., 2018. Estimating arctic sea ice thickness and volume using cryosat-2 radar altimeter data. *Adv. Space Res.* 62, 1203–1225.
- Ulaby, F.T., Moore, R.K., Fung, A.K., 1986. *Microwave remote sensing: Active and passive. Volume 3-From theory to applications.* NASA. URL: <https://ntrs.nasa.gov/search.jsp?R=19860041708>.
- Warren, S.G., Rigor, I.G., Untersteiner, N., Radionov, V.F., Bryazgin, N. N., Aleksandrov, Y.I., Colony, R., 1999. Snow depth on arctic sea ice. *J. Clim.* 12, 1814–1829.
- Wingham, D., Francis, C., Baker, S., Bouzinac, C., Brockley, D., Cullen, R., de Chateau-Thierry, P., Laxon, S., Mallow, U., Mavrocordatos, C., et al., 2006. Cryosat: a mission to determine the fluctuations in earth's land and marine ice fields. *Adv. Space Res.* 37, 841–871.